Systematic investigations into the role of ceramide subclass composition on lipid organization and skin barrier

Nadaban, A.

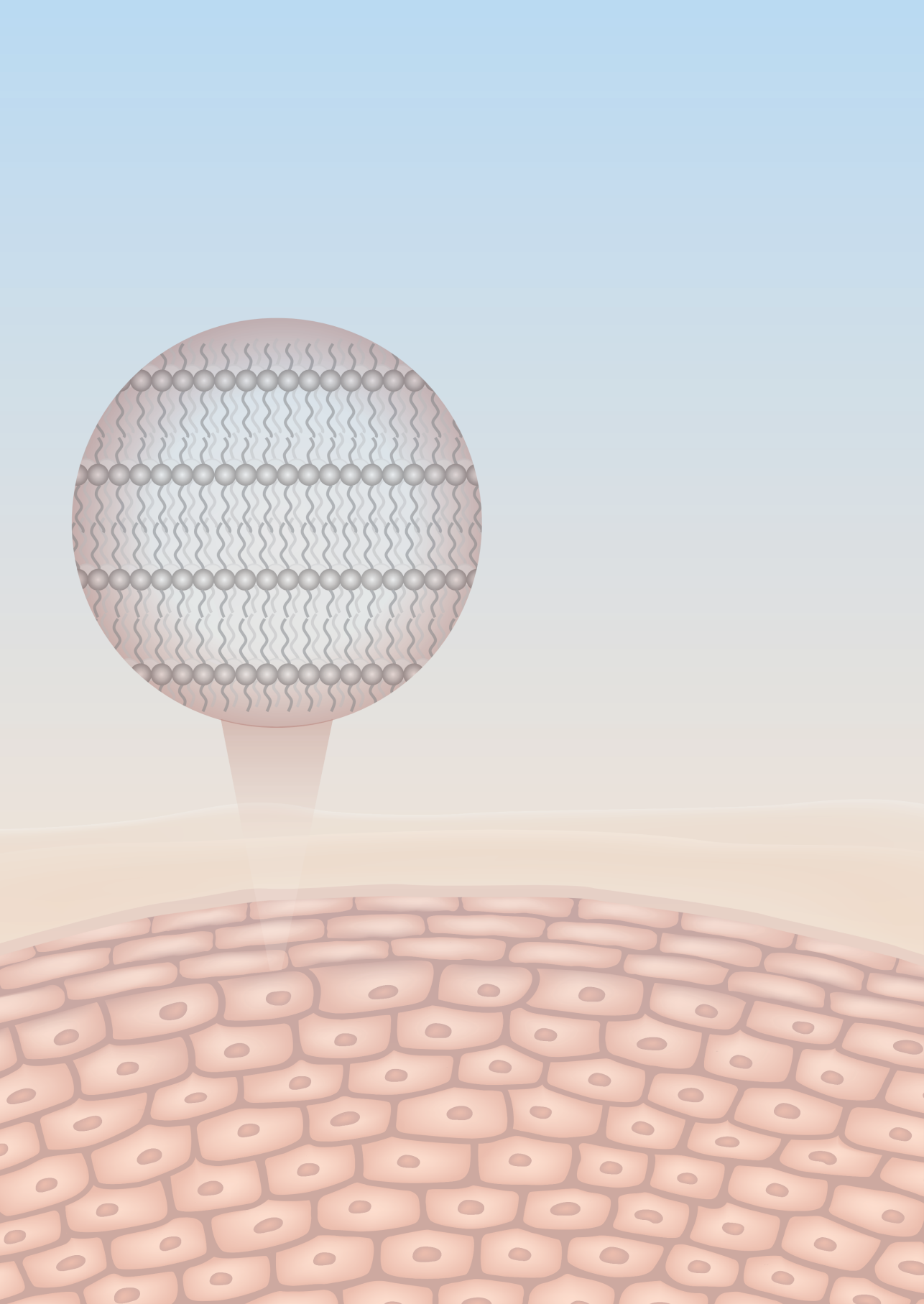

CHAPTER 5

Influence of the sphingosine and phytosphingosine ceramide ratio on the lipid organization in the short periodicity phase

Authors and affiliations:
Andreea Nădăban[1], Dounia El Yachioui[1], Gerrit S. Gooris[1], Robert M. Dalgliesh[2], Marc Malfois[3], Joke A. Bouwstra[1*]

[1]Division of BioTherapeutics, Leiden Academic Centre for Drug Research, Leiden University, Leiden, The Netherlands
[2]ISIS Neutron and Muon Source, Science and Technology Facilities Council, Rutherford Appleton Laboratory, Didcot, United Kingdom
[3]ALBA Synchrotron, Cerdanyola del Vallès, Barcelona, Spain

To be submitted

ABSTRACT

The lipids located in the outermost layer of the skin, known as the stratum corneum (SC), play a crucial role in maintaining the barrier function of the skin. The primary components of the SC lipid matrix are ceramides (CERs), cholesterol (CHOL) and free fatty acids (FFAs). They form two crystalline lamellar phases, the long periodicity phase and short periodicity phase, referred to as the LPP and SPP, respectively. In inflammatory skin conditions like atopic dermatitis and psoriasis, there are alterations in the SC CER composition, such as an increased concentration of a sphingosine-based CER (CER NS), while the concentration of a phytosphingosine-based CER (CER NP) is decreased. In this study, a lipid model was created exclusively forming the SPP, to investigate whether alterations in the CER NS:CER NP molar ratio would affect the lipid organization and whether the arrangement of the lipids is similar as observed in the LPP. Lipid models were prepared using CER NS: CER NP at ratios of 1:2 (mimicking a healthy SC ratio) and 2:1 (ratio observed in inflammatory skin diseases). The CERs were combined with CHOL and FFA C24. The findings indicate that the acyl chains of CER NS and CER NP and FFAs are in close proximity within the SPP unit cell, similarly as observed for the LPP. This also implies that CER NS and CER NP adopt an extended CER conformation in the SPP unit, resembling the arrangement in the inner layer of LPP models. The two compositions showed slightly different hydrogen bonding networks, which might be attributed to intermolecular hydrogen bonding interactions among the CER NP head groups.

INTRODUCTION

Ceramides (CERs) represent one of the main lipid classes of the intercellular regions of the outermost layer of the skin, the stratum corneum (SC). CERs belong to the group of sphingolipids, an important component of biological membranes, which are involved in different biological processes like cell proliferation, differentiation and apoptosis (1, 2). CERs, along with cholesterol (CHOL) and free fatty acids (FFAs), form the highly organized lipid matrix of the SC, which restricts water loss and preventing the permeation of pathogens and other hazardous materials into the body (3-6). The SC lipid matrix does not include phospholipids, in contrast with other biological membranes (7).

The organization of SC lipids is different from other membranes with high CHOL content. In those membranes often a liquid ordered phase is present (8). Lipids in human SC are organized into two coexisting crystalline lamellar phases with repeat distances of ~13 nm and ~6 nm called the long and short periodicity phases (LPP and SPP), respectively (9-11). Previous studies have shown that the esterified ω-hydroxy sphingosine ceramide (CER EOS) plays an important role in the formation of the LPP (12, 13). When CER EOS is not present in the lipid model systems, only the SPP is formed. A gradual increase in CER EOS concentration enhances the formation of the LPP in SC lipid model systems and in SC at the expense of the SPP (14).

Within the LPP and SPP phases, the lipid chains can have different packing densities within the lamellae, referred to as the lateral organization: orthorhombic (ordered phase, very dense packing of lipids), hexagonal (ordered phase, but less dense packing) or liquid phase (disordered lipid packing) (15-17). The human SC lipids mainly adopt an orthorhombic packing, with a smaller fraction of lipids forming a hexagonal packing. Even small liquid domains have been reported in human SC (18).

The SC lipids play a crucial role in the skin barrier function (5, 19). Changes in the SC lipid composition have been reported in inflammatory skin diseases, like psoriasis, atopic dermatitis or seborrheic dermatitis (19-25). Among the different lipid compositional changes, the altered ratio of the CERs containing non-hydroxy acyl chains linked to a sphingosine chain (CER NS) and a phytosphingosine chain (CER NP) is often encountered in diseased SC, and it was reported to correlate with an impaired skin barrier (23, 25, 26). The effect of the CER NS:CER NP molar ratio on the lipid organization and barrier function was recently studied using a lipid model that formed exclusively the LPP (27). The aim of this study was to investigate the effect of a variation of this ratio in a lipid model of which the lipids form only the SPP (in the absence of CER EOS).

The study was performed using lipid models that mimic important aspects of the SC lipid organization. Previously, it was shown that lipid models consisting of isolated CERs (extracted from porcine or human SC) mixed with CHOL and FFAs can mimic the unique lamellar organization of the SC lipids (28-30). Moreover, replacing the isolated porcine or human CERs with their synthetic counterparts did not affect the lamellar phase behavior

of the lipid models, which still mimicked the native SC lipid organization (31-35). The CER composition of lipid models forming only the SPP varied in different studies from a mix of CER subclasses alongside CHOL and FFAs, to systems which only included a single CER subclass, with most of the studies focusing on CER NS (36-41). A similar lamellar and lateral organization of the lipids was reported for the models prepared with five different CER subclasses and models with only CER NS, mixed with CHOL and FFAs. Using lipid models with a limited number of components offers the possibility of a more detailed analysis due to the possibility to use deuterated lipids.

In this study we used the CER NS: CER NP molar ratio of 1:2 (mimicking the ratio observed in healthy SC) and 2:1 (an approximate ratio corresponding to severe inflammatory skin diseases) (23), mixed with CHOL and FFA C24. The lamellar organization, the lipid packing and lipid chain interactions were examined, as well as the hydrogen network formed in the systems.

MATERIALS AND METHODS

Materials

The CERs used in this study were *N*-(tetracosanoyl)-sphingosine (CER NS C24), *N*-(tetracosanoyl)-phytosphingosine (CER NP C24) and these two CERs with perdeuterated acyl chain (CER NSd47 and CER NPd47), kindly donated by Evonik (Essen, Germany) (Figure S1). CER NS with the sphingosine chain terminally deuterated (CER NSd7) was acquired from Avanti Polar Lipids (Alabama, USA). CHOL, lignoceric acid (FFA C24), D_2O and the acetate buffer salts were obtained from Sigma-Aldrich-Chemie GmbH (Schnelldorf, Germany). The perdeuterated FFA C24 (DFFA C24) was purchased from Arc Laboratories B.V. (Apeldoorn, The Netherlands). All organic solvents were of analytical grade, acquired from Biosolve B.V. (Valkenswaard, The Netherlands). The Nuclepore track-etched membranes were purchased from Whatman (Kent, UK). The milli-Q water was of Millipore quality.

Lipid model compositions and preparation

The lipid models were prepared in equimolar ratio of CERs, CHOL and FFA C24 (1:1:1). Two ratios of CER NS: CER NP were included in this study: 1:2 and 2:1 (Table 1). For the Fourier-transform infrared spectroscopy (FTIR) studies, similar models were prepared with DFFA C24, CER NSd47 and/or CER NPd47. For Neutron diffraction studies, a model with CER NSd7 was prepared (SPP NS:NP 2:1). All of the models studied are presented in Table 1.

Table 1. Sample compositions and abbreviations of the lipid models studied

Lipid model	Composition	Molar ratios
SPP NS:NP 1:2	CER NS C24: CER NP C24: CHOL: FFA C24	0.33:0.66:1:1
SPP NS:NP 2:1	CER NS C24: CER NP C24: CHOL: FFA C24	0.66:0.33:1:1
SPP NSd47:NPd47:DFFA 1:2	CER NSd47: CER NPd47: CHOL: DFFA C24	0.33:0.66:1:1
SPP NSd47:NPd47:DFFA 2:1	CER NSd47: CER NPd47: CHOL: DFFA C24	0.66:0.33:1:1
SPP NS:NPd47:DFFA 1:2	CER NS: CER NPd47: CHOL: DFFA C24	0.33:0.66:1:1
SPP NS:NPd47:DFFA 2:1	CER NS: CER NPd47: CHOL: DFFA C24	0.66:0.33:1:1
SPP NSd47:NP:DFFA 1:2	CER NSd47: CER NP: CHOL: DFFA C24	0.33:0.66:1:1
SPP NSd47:NP:DFFA 2:1	CER NSd47: CER NP: CHOL: DFFA C24	0.66:0.33:1:1
SPP NSd7:NP 2:1	CER NSd7: CER NP: CHOL: FFA C24	0.66:0.33:1:1

First, to prepare the samples, the required amount of each individual lipid was dissolved in chloroform: methanol (2:1, v/v), at a concentration of 5 mg/mL. For the samples used for FTIR studies, 1 mg of the lipid composition was sprayed on an AgBr window over a 10 x 10 mm area. The samples for X-ray studies were dissolved in hexane: ethanol (2:1, v/v) and then sprayed on a Nuclepore polycarbonate membrane, over an area of 2 x 3 mm. During spraying, a Camag Linomat IV sprayer (Muttenz, Switzerland) was used with a spraying rate of 14 s/µL. For the neutron diffraction measurements, 10 mg of lipids dissolved in chloroform: methanol (2:1, v/v) were sprayed on a silicon substrate over an area of 1.2 x 3.8 cm^2, using the same spraying conditions. All samples were equilibrated at 95 °C for 65 min, then slowly cooled to room temperature over 50 min. Lastly, the samples were hydrated with either deuterated acetate buffer (pH 5.0, for FTIR studies) or D_2O/H_2O buffer (at three ratios, 8%, 50% and 100% D_2O) for neutron studies. This hydration occurred at 37 °C for at least 12 hours. Prior to the X-ray measurements, the lipid samples were maintained at 80% relative humidity for at least 24 h.

FTIR measurements

The FTIR data were collected on a PerkinElmer Frontier FTIR (PerkinElmer, Waltham, USA), with a nitrogen cooled mercury cadmium telluride detector. The sample compartment was purged with a continuous flow of dry air to remove moisture. Each spectrum consists of 77 interferograms with a resolution of 1 cm^{-1} (wavenumber). The samples were measured in the wavenumber range of 500-4000 cm^{-1}, between 10 and 90 °C at a heating rate of 4 min/°C. The spectra were extracted using TimeBase (PerkinElmer, Waltham, USA) and processed using Spectrum (Perkin Elmer, Waltham, USA). The data was deconvoluted using γ = 2.2 and a smoothing factor of 76.7. For all lipid compositions measurements were carried out in triplicate.

By analyzing the CH_2 symmetric stretching vibrations (ν_sCH_2), information about the lateral packing and the phase transition of the lipid chains was acquired. The ν_sCH_2 vibrations are observed at ~2849 cm^{-1} and the CD_2 symmetric stretching vibrations at

~2090 cm^{-1} ($\nu_s CD_2$). The mid-phase transition temperature is defined as the temperature at which the lipids are transitioning from orthorhombic to hexagonal packing (T_mO-H) or from hexagonal to liquid (T_mH-L) packing. It was calculated by using the linear regression curve fitting method described elsewhere (39). The lipid chain packing is determined by examining the CH_2 and CD_2 scissoring vibrations (δCH_2, wavenumber range: 1462-1473 cm^{-1}; δCD_2, wavenumber range: 1085-1095 cm^{-1}). Python scripts were used for determination of the δCH_2 and δCD_2 peak positions (fitting Lorentzian peaks) and peak heights. A peak height ratio (OR/MID) was then calculated as the ratio of the average peak height of the two orthorhombic peaks and the height of the central peak. Statistical analyses were performed using Graphpad Prism (v.8) to determine the statistical significance of the mid-phase transition temperatures and scissoring peak splitting of the different compositions (unpaired t-test, significance level set at $P<0.05$). For the amide vibrations (amide I ~1650 cm^{-1} and amide II ~1550 cm^{-1}) the peak positions were determined by peak fitting using the Fityk software (42).

X-ray diffraction measurements

Small-angle X-ray diffraction (SAXD) measurements were performed at the NCD-SWEET beamline (ALBA Synchrotron, Barcelona, Spain), using a Pilatus 1M detector with a pixel array of 981 × 1043, each pixel: 172 × 172 μm^2. The sample to detector distance was 2.148 m, beam wavelength was 0.999 Å. The temperature for the measurements was 23 °C and the samples were scanned for 20 s. Silver behenate was used for calibration of the setup. The one-dimensional SAXD profiles of the scattering intensity as a function of the scattering vector (q) were obtained after the integration of the two-dimensional scattering plot, over a 90° segment from the beam center. The scattering vector (q) is calculated using the formula: $q = (4\pi \sin\theta)/\lambda$, where θ represents the scattering angle and λ is the wavelength. The positions of the n^{th} order diffraction peak (q_n) were determined by peak fitting with the Fityk software, using the Pearson VII function (42). Least squares fitting was used to calculate the repeat distance of the lamellar phase (d), as $d = 2n\pi/q_n$. For peaks that correspond to unknown phases (i.e., not part of a lamellar phase), the spacing at the peak position q was calculated as $spacing = 2\pi/q$.

Neutron diffraction measurements

The small-angle neutron diffraction measurements were performed on the LARMOR instrument at ISIS Neutron and Muon Source (Rutherford Appleton Laboratory, UK). The wavelength range of the neutron beam (with a size 1 x 30 mm) was 1 – 12.5 Å. The distance between the detector and the sample was 4.4 m. The detector was set at 2θ angle of 5° to the direct beam (area covered 664 × 600 mm; pixel size 4 × 8 mm). The angle of the sample to the beam was 2.5°. An aluminum chamber was used for the sample environment, which allowed a constant temperature of the windows of the chamber at

42°C to prevent condensation. An empty chamber was used for a background measurement, which was subtracted from each sample. The samples were measured for 4 h each (40 μA/h accelerator proton charge) at 25 °C for each of the three hydration buffer ratios. A direct beam measurement was used for the normalization to the incident flux shape and the detector efficiency.

To monitor the normalized intensity as a function of the scattering vector (*q*), the neutron data was reduced using the Mantid software framework (43). The resulting *q*-range was 0.032 – 0.991 nm^{-1}. The Bragg equation was used to convert the scattering angle (2θ) to *q* as $q = 4\pi\ sin\theta\ /\ \lambda$. Based on the positions of the equidistant Bragg peaks, the repeat distance (*d*) of the lamellar phase was calculated as $d = 2\pi n/q_n$, with *n* representing the diffraction order number of the peak at the position q_n.

The intensity of each diffraction order was obtained by fitting the Bragg peaks (Fityk software, with a Pearson VII function) (42). Next, the structure factor amplitude for each diffraction order ($|F_n|$) was determined using the formula $\left|F_n\right| = A_n\sqrt{LI_n}$, where L is the Lorentz correction factor, that can be assumed equal to *q*, due to the high degree of lipid lamellae orientation (44). A_n, the correction factor for the sample absorption, was calculated with the formula below, where *l* is the thickness of the lipid sample and μ is the linear attenuation coefficient (45):

$$A_n = \frac{1}{\sqrt{\frac{sin\theta}{2\mu l}\left(1-e^{\frac{-2\mu l}{sin\theta}}\right)}}$$

The contrast variation method with D_2O/H_2O buffer levels (100%, 50%, and 8%) was used to determine the phase signs of the water profile, which are obtained from the positive or negative signs of the slopes of the linear correlation of the absolute structure factors of the samples hydrated at 100% and 8% D_2O/H_2O (46). Assuming water is associated with the hydrophilic head groups located at the boundary of the unit cell, we used the following phase signs combination: - + - + for the four diffraction orders detected in the samples. Next, the F_n with the corresponding phase signs are plotted as a function of the D_2O/H_2O buffer ratio (Figure S2), resulting in a linear fitting for each diffraction order.

The scattering length density profile (SLD) of the SPP unit was obtained by Fourier reconstructions using the structure factor values and the phase signs with the following equation:

$$\rho(x) = F_0 + 2\sum_{n=1}^{n_{max}} F_h\ cos\left(\frac{2\pi nx}{d}\right)$$

where *x* is the distance in the unit cell and *x* = 0 represents the center of the unit cell. F_0 represents the scattering density per unit volume. This was calculated using the lipid sample density and its chemical composition (one water molecule per lipid was included) (47). The SLD profile of the deuterated moiety is determined from the difference between the SLD profile of the deuterated sample and the SLD profile of the protiated sample (both

hydrated at 8% D_2O/H_2O) and this net SLD profile indicates the location of the deuterated part of the lipid chain.

The SLD data was placed on a "relative absolute" scale using a scaling factor, as described previously (44, 48, 49). For the SPP NSd7:NP 2:1 sample, in the SLD profile of the NSd7 chain, the peak area (SLD_a) and peak height (SLD_h) were fitted. The peak area obtained from the subtraction of the SLD profiles of the SPP NS:NP 2:1 sample from the SPP NSd7:NP 2:1 sample, represents the scattering of the deuterium atoms from the CER NS sphingosine chain (SLD_{dif}). The relative absolute SLD profile ($SLD_{correct}$) was calculated as:

$$SLD_{correct} = \frac{SLD_h * SLD_{dif}}{SLD_a}$$

The scaling factor that was then applied to the structure factor values (F_n) was calculated as the ratio between $SLD_{correct}$ and SLD_h values.

RESULTS AND DISCUSSION

Lamellar organization of the two models

The lamellar organization of the two lipid models with CER NS:CER NP ratio 1:2 and 2:1 was examined with SAXD. Figure 1 shows the diffraction profiles of the two systems. The SPP NS:NP 2:1 system is characterized by a series of equidistant peaks, indicating a lamellar phase with a repeat distance of 5.4 nm, the SPP. The only peak that is not assigned to the SPP is phase-separated crystalline CHOL (positioned at q = 1.8 nm^{-1}). The diffraction profile of the SPP NS:NP 1:2 model also shows a series of three equidistant peaks with the repeat distance of 5.4 nm, indicating the formation of the SPP. However, the SAXD profile of this model also shows two other phases indicated in Figure 1. The hash symbols designate a lamellar phase with a d-spacing twice that of the SPP (d = 10.8 nm, first diffraction peak at q = 0.58 nm^{-1}), which has its other diffraction orders overlapping the first, second and third SPP peaks. There are previous reports about a lamellar phase with ~10.6 nm repeat distance in compositions that included CER NH C24 (50, 51), CER NS C24 (52) (Shamaprasad et al. unpublished) and a mixture of CER NS C24/CER NH C24 (53). This phase with a suggested double-bilayer structure was first reported in 1993, but was not considered representative for SC and it was suggested to be an artifact of the sample preparation technique used (54).

The plus symbol in Figure 1 identifies an unknown phase with a peak at a q = 1.4 nm^{-1} (spacing 4.4 nm), which has been observed previously in other compositions and it was suggested that this is a crystalline phase containing CER NP C24 (55). Dahlen et al. reported that pure CER NP C24 needs to be orthorhombically packed and it would adopt a V-shape conformation with a tilt angle of ~ 41°. A spacing of 4.4 nm was also reported in an equimolar model with CER NP C24, CHOL and FFA C24, and the 4.4 nm phase was suggested to represent the V-shape arrangement of CER NP (56).

Unlike the denoted phase separation for the SPP NS:NP 1:2 model, lipid models forming the LPP (the same ratio between the lipid, but with the addition of CER EOS) did not form multi-phase systems even when the CER NS:CER NP molar ratio was 1:2 (27). This suggests that the addition of CER EOS improves the miscibility of the lipids in the model (36, 57).

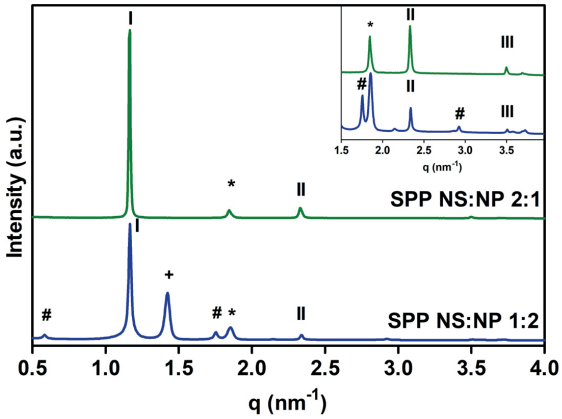

Figure 1. SAXD profiles of the SPP NS:NP 1:2 (blue, lower) and SPP NS:NP 2:1 (green, upper) models. The SPP diffraction orders are indicated with Roman numbers, the asterisk (*) indicates phase-separated CHOL peaks, the hash (#) indicates the peaks corresponding to a lamellar phase with a d-spacing of 10.8 nm and the plus (+) indicates an unknown peak. The top-right panel shows an expanded view of the profile for the *q* range 1.5 – 3.6 nm^{-1}. Data represents an average of 2 measurements.

Lateral organization of the models

Next, the lateral lipid organization was examined using FTIR. The δCH_2 vibrations for the protiated SPP NS:NP 1:2 and SPP NS:NP 2:1 models show two clear peaks at approximately 1462 cm^{-1} and 1473 cm^{-1} (characteristic for orthorhombic packing) and a smaller central peak at 1467 cm^{-1} (attributed to the hexagonal packing of the lipids) (Figure 2A). Peak fitting with Python scripts was used to determine the accurate δCH_2 peak position, the δCH_2 peak splitting (distance between the two peaks caused by an orthorhombic packing), and then the peak height ratio of the average of the two orthorhombic peaks and the hexagonal middle peak (OR/MID). While the δCH_2 peak splitting distance was the same for both models (10.3 ± 0.08 cm^{-1}, Table 2), the SPP NS:NP 1:2 model had a significantly higher central peak relative to the two orthorhombic peaks, and thus a lower OR/MID ratio (1.9 ± 0.1), than the SPP NS:NP 2:1 model (OR/MID ratio 2.3 ± 0.1). The δCH_2 vibrations suggest that both models adopt primarily an orthorhombic packing, however, a small fraction of lipids forms a hexagonal packing, which is higher in the SPP NS:NP 1:2 model. In Figure S3, the δCH_2 vibrations are provided in the 10-50°C temperature range. These vibrations indicate an orthorhombic to hexagonal phase transition.

The thermotropic curves of the $\nu_s CH_2$ vibrations are shown in Figure 2B. At 10°C the $\nu_s CH_2$ wavenumber is <2849 cm^{-1} indicating a high conformational order, while at 32°C there is a transition to a less ordered system, indicated by the increase of the $\nu_s CH_2$ wavenumber. Correlating the $\nu_s CH_2$ vibrations with the observations from the δCH_2 vibrations (Figure S3), this corresponds to the transition from the orthorhombic to hexagonal lipid packing. The mid-phase transition temperatures were similar for the two models, as indicated in Table 2. When the temperature is further increased, another transition can be observed at ~70°C as depicted in Figure 2B, from hexagonal lipid packing to a liquid phase. The difference between the mid-phase transition temperatures (T_m H-L) of the two models is statistically significant ($P<0.05$), as the SPP NS:NP 2:1 model showed a sharper transition with T_m H-L = 70.8 ± 1.8°C, than the transition observed for the SPP NS:NP 1:2 model with T_m H-L = 74.6 ± 0.4 °C (Table 2).

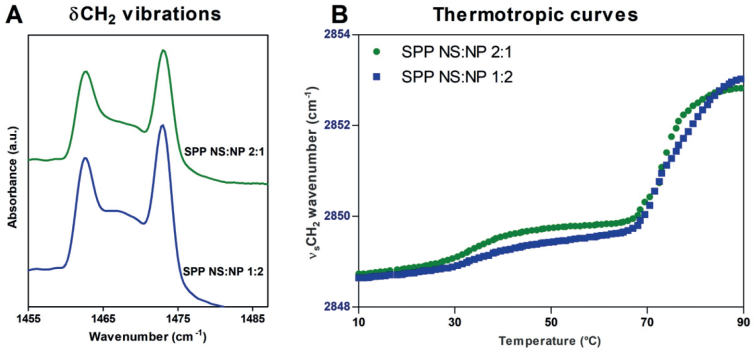

Figure 2. (A) δCH_2 vibrations of the two protiated models, measured at 10°C. (B) Thermotropic curves of the SPP NS:NP 1:2 and 2:1 models, showing the $\nu_s CH_2$ wavenumbers as a function of temperature in the range 10-90°C.

Table 2. δCH_2 peak splitting distance, δCH_2 peak height ratio (OR/MID) of the two SPP models, at 10°C, and the mid-phase transition temperatures (T_m O-H and T_m H-L). Data is shown as an average of 3 measurements for each composition ± SD.

Lipid model	δCH_2 peak splitting ± SD	OR/MID peak height ratio ± SD	T_m O-H ± SD (°C)	T_m H-L ± SD (°C)
SPP NS:NP 1:2	10.3 ± 0.1	1.9 ± 0.1	32.4 ± 0.7	74.6 ± 0.4
SPP NS:NP 2:1	10.3 ± 0.1	2.3 ± 0.1	32.6 ± 1.6	70.8 ± 1.8

Increased hydrogen bonding in the SPP NS:NP 1:2 model

The presence of the hydroxyl and the amide group in the CER structure allows them to act as both a hydrogen bond donor and acceptor. The amide I (~1650 cm^{-1}) and amide II (~1550 cm^{-1}) vibrations measured with FTIR were used to examine hydrogen bonding in the CER head group regions. The amide I band results mainly from the C=O stretching vibration and the amide II reflects primarily the N-H bending vibration and C-N stretching

vibration. Stronger hydrogen bonding can be concluded when there is a lower frequency of the amide I and a higher frequency of amide II vibrations (i.e., the positions of the two amide vibrations are closer) (58, 59). The amide I vibrations are split into two components in the SPP NS:NP 1:2 model, with a peak positioned at 1612.8 ± 0.8 cm^{-1} and another peak at 1640.7 ± 0.5 cm^{-1} (Figure 3). In the spectrum of the SPP NS:NP 2:1 model, the amide I frequency is characterized by a broad peak, centered at 1634.7 ± 2.5 cm^{-1}. The peak corresponding to the amide II band has the same position in both models (1547.9 ±0.3 cm^{-1} for SPP NS:NP 1:2 and 1548.1 ± 0.6 cm^{-1} for SPP NS:NP 2:1 model).

Comparing the two systems from Figure 3, the SPP NS:NP 1:2 system displayed a lower wavenumber of the amide I vibration and a shorter distance to the amide II peak, indicating stronger hydrogen bonding compared to the SPP NS:NP 2:1 model. The intermolecular hydrogen bonding between two CER NP headgroups might contribute to the shift in position and the doublet of the amide I frequency, as it was reported to occur for pure CER NP (60). This difference in the hydrogen bonding of the two models is in agreement with other studies, as a stronger hydrogen bonding determined by CER NP compared to CER NS was previously reported for single component systems, as well as in SPP and LPP models (59-61).

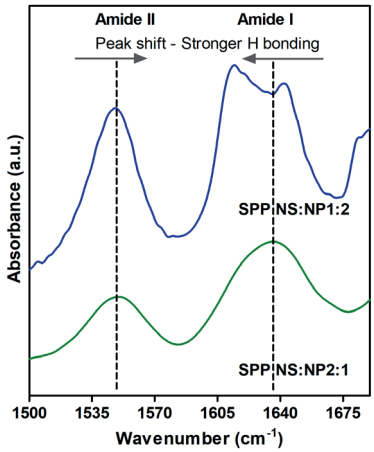

Figure 3. FTIR spectrum of the region 1500 – 1680 cm^{-1} at 10°C, showing the amide I and II frequencies in the SPP NS:NP 2:1 (green, bottom) and SPP NS:NP 1:2 model (blue, top). The shift of the two amide peaks indicates a difference in the hydrogen bond network in the system.

Thermotropic behavior indicates phase separation in SPP NS:NP 1:2 model

To further investigate the lipid mixing of the models, some of the lipids were replaced with their deuterated counterparts: perdeuterated acyl chain of CER NP and/or CER NS and perdeuterated FFA C24. The thermotropic curves of these models (Figure 4) show different behavior of the two SPP models (1:2 and 2:1 ratios). The SPP NS:NP 2:1 models are characterized by sharp transitions from hexagonal to liquid phase, similar to the

protiated sample discussed previously (Figure 2B). Moreover, a similar thermotropic response of the ν_sCH_2 and ν_sCD_2 vibrations is detected for the SPP NS:NP 2:1 models. This indicates that the hexagonal to liquid phase transitions of the protiated and deuterated lipids occur in the same temperature range when the temperature is increased; thus, the lipid chains are well mixed in the model.

Figure 4 shows that the SPP NS:NP 1:2 models have a larger hexagonal to liquid phase-transition temperature range than the SPP NS:NP 2:1 model. On average, this phase transition of the SPP NS:NP 1:2 models occurs over a 20°C temperature range, while for the SPP NS:NP 2:1 models, this is 12°C. However, the protiated and deuterated chains of both SPP NSd47:NPd47:DFFA 1:2 and SPP NS:NPd47:DFFA 1:2 models melt in the same temperature range (Figure 4A and B), indicating that the protiated and deuterated lipids have a similar thermotropic behavior. The SPP NSd47:NP:DFFA 1:2 model (Figure 4C) shows different ranges in transition temperature for the deuterated and protiated lipids, indicating that lipid domains of different composition are formed in this model.

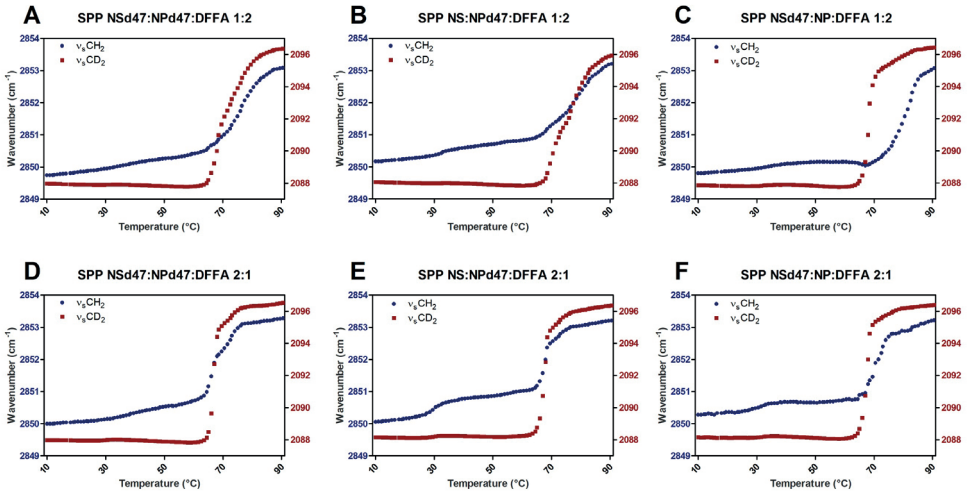

Figure 4. Thermotropic curves of the ν_sCH_2 and ν_sCD_2 vibrations for the SPP NS: NP 1:2 (A-C) and 2:1 (D-F) ratio models with different deuterated chains. The wavenumbers of the ν_sCH_2 and ν_sCD_2 peak positions (left and right y-axis, respectively) are plotted in the 10-90°C temperature range. Data shown as an average of 3 measurements for each composition.

The mid-transition temperature of the deuterated and protiated chains in the SPP NSd47:NP DFFA 1:2 deuterated models is significantly different, as shown in Table 3. This suggests that the lipids in this mixture do not mix homogenously. The SAXD data of the SPP NS:NP 1:2 model showed an unidentified phase with a spacing at 4.4 nm, which as discussed above, might contain primarily CER NP. The differences in the mid-transition temperatures between the protiated and deuterated lipids could be caused by this crystalline CER NP rich phase. Due to the presence of a high concentration of CER NP, it is expected to have a delayed onset of the melting process of the protiated chains. This is in

agreement with the observation that in the SPP NSd47:NPd47:DFFA 1:2 model the protiated chains do not show a delay in the hexagonal - liquid transition (Figure 4D).

There is only a weak phase transition from orthorhombic to hexagonal packing of the protiated lipid chains in most compositions shown in Figure 4, as in most compositions the $\nu_s CH_2$ wavenumber shows a slight and steady increase up to 50°C. This is an indication that the protiated lipids (CHOL, sphingosine and phytosphingosine chains) adopt primarily a hexagonal organization (except in the SPP NS:NPd47:DFFA 2:1 model). Unlike these SPP systems, in the LPP models studied recently, clear transitions from orthorhombic to hexagonal phases were noticed in the thermotropic plots of the deuterated samples (27). It has been previously reported that CER EOS may enhance the formation of the orthorhombic phase, as the long acyl chains of CER EOS might increase the van der Waals interactions (36, 62). Thus, the presence of CER EOS acyl chains could be a possible explanation for the aforementioned differences between these SPP systems and the LPP models.

Table 3. The mid-phase transition temperature of the hexagonal – liquid phase (T_m H-L), the δCD_2 peak splitting and the OR/MID δCD_2 peak height ratio of the deuterated SPP models. The scissoring peak data is calculated at 10°C. Data represents an average of 3 measurements for each composition with the standard deviations.

Lipid model	T_m H-L ± SD (°C)	δCD_2 peak splitting ± SD (cm^{-1})	OR/MID peak height ratio ± SD
SPP NSd47:NPd47:DFFA 1:2	75.3 ± 0.6	7.2 ± 0.1	5.3 ± 0.3
SPP NSd47:NPd47:DFFA 2:1	68.6 ± 0.6	7.2 ± 0.1	5.3 ± 0.4
SPP NS:NPd47:DFFA 1:2	76.8 ± 0.4	5.9 ± 0.1	3.3 ± 0.2
SPP NS:NPd47:DFFA 2:1	68.1 ± 0.9	5.0 ± 0.1	2.9 ± 0.2
SPP NSd47:NP:DFFA 1:2	80.7 ± 1.4	6.4 ± 0.1	2.7 ± 0.2
SPP NSd47:NP:DFFA 2:1	74.5 ± 0.9	6.2 ± 0.1	3.4 ± 0.2

At 32°C (skin temperature), the wavenumbers of the $\nu_s CH_2$ vibration in the SPP NSd47:NPd47:DFFA 1:2 and 2:1 systems are 2850.1 ± 0.2 cm^{-1} and 2850.2 ± 0.1 cm^{-1}, respectively. The stretching wavenumber at this temperature indicates that the protiated sphingosine and phytosphingosine chains and CHOL have less conformational ordering than at 10°C. The conformational disordering of the sphingosine chain of CER NS was previously reported by Engberg et al., who labeled this phase as a fluid, highly mobile phase, based on the ^2H NMR results (40). However, a clear distinction should be made regarding the packing of the sphingosine chain of CER NS, as in FTIR terminology a fluid disordered phase is characterized by a $\nu_s CH_2$ wavenumber >2853 cm^{-1} and a $\nu_s CD_2$ wavenumber >2096 cm^{-1}. In the Engberg et al. study, the $\nu_s CH_2$ wavenumber of the deuterated sphingosine CER NS chain is ~2089.5 cm^{-1} (40), which indicates some conformational disordering, but not a fluid phase as detected by FTIR.

The linear conformation of CER NS and CER NP is similar to LPP models

The mixing of the lipid chains is further examined using the scissoring vibrations. The results are provided in Figure 5, which shows the splitting of the δCD_2 and δCH_2 vibrations in the FTIR spectra of the various compositions. In an orthorhombic packing, the hydrocarbon lipid chains are packed tightly, allowing short-range coupling of the CH_2-CH_2 groups, interaction of neighboring CH_2 groups, resulting in a peak splitting of the δCH_2 vibrations. The size of the orthorhombic domains determines the δCH_2 peak splitting distance, with a maximum peak splitting distance of 7.3 ± 0.1 cm^{-1} obtained when the lipid domains are around 100 chains (63, 64). Similarly, when deuterated lipid chains are included in the models, the CD_2-CD_2 chains interact if they are neighboring, resulting in two separated δCD_2 peaks at ~1085 and ~1092 cm^{-1}. However, if the deuterated chains are neighboring protiated chains that participate in the same lattice, CD_2-CH_2 interactions occur, resulting in the loss of the CD_2-CD_2 chain frequency coupling. A central peak is formed in both the δCD_2 vibrations (~1088 cm^{-1}) and δCH_2 vibration (~1468 cm^{-1}), resulting in a shallower depth between the two orthorhombic peaks.

Large deuterated domains are formed in the SPP NSd47:NPd47:DFFA models (1:2 and 2:1 ratios; Figure 4 A,D), as the distance of the δCD_2 peak splitting is 7.2 ± 0.1 cm^{-1} in both compositions (Table 3). These values are close to the maximum δCD_2 peak splitting value obtained for pure DFFA C24 (7.3 ± 0.1 cm^{-1}), which suggests that the acyl chains of CER NS and CER NP are neighboring the DFFA chains. An indication of the number of CH_2-CD_2 interactions is the peak ratio of the two orthorhombic peaks and the central peak (OR/MID ratio). This ratio was calculated by peak fitting. The OR/MID ratio values obtained for this model are very high, indicating that the CD_2-CD_2 chain interactions are predominant in the system (Table 3).

To further investigate the deuterated lipid domains in the SPP models, CER NSd47 was replaced by the protiated CER NS in the SPP NS:NPd47:DFFA (1:2 and 2:1) models. Both models indicate that smaller deuterated lipid domains are present (Table 3). The OR/MID peak height ratios of these models are significantly decreased compared to the SPP NSd47:NPd47:DFFA models, indicating that in the SPP NS:NPd47:DFFA models there are significantly less CD_2-CD_2 chain interactions and more CH_2-CD_2 interactions. This confirms that the deuterated acyl chain of CER NS is part of the deuterated domains formed in the SPP NSd47:NPd47:DFFA models. Neighboring of these chains is only possible when CER NS and CER NP are present in a linear arrangement in the SPP models, with the acyl chain and (phyto)sphingosine chain on either side of the headgroup. The difference in the δCD_2 peak splitting values between the SPP NS:NPd47:DFFA 1:2 and SPP NS:NPd47:DFFA 2:1 models (Table 3) are probably only caused by the different concentrations of the deuterated CER NP in the models. Next, CER NPd47 was replaced by its protiated counterpart resulting in the SPP NSd47:NP:DFFA 1:2 and 2:1 models. The conclusions of the SPP NS:NPd47:DFFA models also apply to the SPP NSd47:NP:DFFA

models: smaller deuterated lipid domains than the SPP NSd47:NPd47:DFFA models and a linear arrangement of CER NS and CER NP.

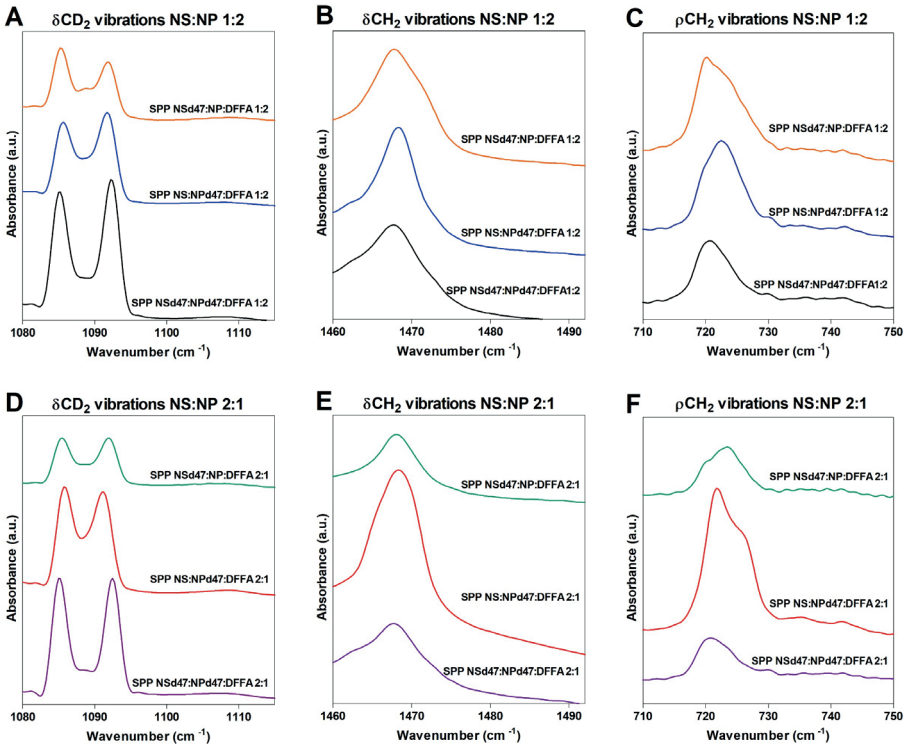

Figure 5. δCD_2 vibrations (A,D), δCH_2 vibrations (B,E) and ρCH_2 vibrations (C,F) for the partially deuterated models SPP NSd47:NP:DFFA, SPP NS:NPd47:DFFA and SPP NSd47:NPd47:DFFA with the CER NS:CER NP ratio 1:2 (top row of panels) and 2:1 (bottom row), measured at 10°C.

The linear arrangements of CER NS and CER NP are also observed in LPP models with the same composition (CER EOS: CER NS: CER NP: CHOL: FFAC24) (27, 46). Studies of the LPP models using neutron diffraction and the peak splitting observed in FTIR measurements both indicate that the acyl chains of CER NS and CER NP are neighboring FFA C24, regardless of the CER NS:CER NP molar ratio, similar to the results observed in the SPP model in the present study. The linear conformation of CER NS was reported in previous studies using LPP models with different compositions (65, 66) and SPP models (38, 40) (Shamaprasad et al. unpublished), however, the conformation of CER NP in SPP models was often debated, with different possible arrangements suggested, such as V-shape (55, 56) or hairpin conformation (67). The V-shape configuration was detected in a phase with a repeat distance of 4.3 nm, likely representing phase-separated CER NP. In the

SPP with 5.4 nm repeat distance, CER NP is suggested to be arranged in either hairpin or extended conformations.

When CER NS and CER NP are in a linear conformation, the acyl chains of CER NS and CER NP are neighboring the FFAs, as discussed above, consequently the sphingosine and phytosphingosine chains of the CERs and CHOL are also neighboring in another part of the repeating unit of the SPP. The δCH_2 vibrations of the deuterated SPP models (SPP NSd47:NPd47:DFFA, SPP NSd47:NP:DFFA, SPP NS:NPd47:DFFA 1:2 and 2:1 ratios) are characterized by the presence of a singlet at 1468 cm^{-1} (Figure 5B,E). As the sphingosine chains and CHOL are neighboring, an absence of the doublet in the δCH_2 vibrations indicates that there is almost no orthorhombic packing of the these protiated lipid chains. To investigate this further, the rocking vibrations are also examined to provide more information about the chain packing (Figure 5C,F). A broad single peak is observed at ~720 cm^{-1} for the SPP NSd47:NPd47:DFFA models (1:2 and 2:1 ratios), as well. The singlet in these two models suggest that the (phyto)sphingosine chains and the CHOL are mainly hexagonally packed. The sphingosine chain of CER NS and CHOL were previously reported to form a dynamic phase with a high mobility in SPP models (40) (Shamaprasad et al. unpublished).

Neutron diffraction shows the symmetric structure of the SPP

For the neutron diffraction measurements, the SPP NS:NP 2:1 model was selected to avoid the overlap of the diffraction peaks with peaks from the unknown phases observed in the SPP NS:NP 1:2 model. The SLD profiles of the protiated SPP NS:NP 2:1 sample, hydrated at 8% and 100% D_2O, are shown in Figure 6A. The profile of the protiated sample is characterized by a high SLD value at the borders of the unit cells, indicating that the lipid head groups are located at the boundary of the unit cell.

The SLD profile of the CER NSd7 chain (in the SPP NSd7:NP 2:1 sample) displays two peaks at the position of ~0.7 nm from the unit cell center (~2 nm from the unit cell border) (Figure 6B). A linearly extended sphingosine chain of C18 chain length corresponds to a length of ~ 1.9 nm, assuming a C-C bond length of 0.125 nm and 15 C-C bonds (66). Thus, the SLD profile intensity shows the location of the NSd7 terminally deuterated chain with the CER head group at the unit cell border. The proposed arrangement is schematically shown in Figure S4.

The neutron diffraction data indicates a symmetric structure of the SPP unit, also for CER NSd7 chain, which is located at both head group regions. This contrasts with the FTIR results that suggest an asymmetric arrangement, also of CER NS. The FTIR results of the SPP NS:NP 2:1 system indicate that the acyl chains of CER NS, CER NP and FFA C24 are neighboring, as shown by the large lipid domains indicated by the scissoring vibration measurements. This suggests an asymmetric arrangement in the SPP profile: on one side the CHOL neighboring the (phyto)sphingosine chains, while FFAs are positioned next to the acyl chains of the CERs. However, while the FTIR scissoring vibrations provide

information about the domain sized formed, neutron diffraction shows the overall mean orientation of the lipids in the system. If the asymmetric arrangement is present in a mirrored orientation with lipids domains larger than 100 chains, FTIR will detect an asymmetric arrangement (based on the interactions between neighboring lipid chains), while neutron diffraction will detect this as a symmetric arrangement, as this technique provides information based on the sum of the two mirror arrangements (Figure S4).

This study shows for the first time in the same SPP composition that the neutron diffraction data indicate a symmetric arrangement, while the FTIR data can only be explained by an asymmetric arrangement. Engberg et al. already proposed an asymmetric arrangement solely based on FTIR data for model containing a single CER (40).

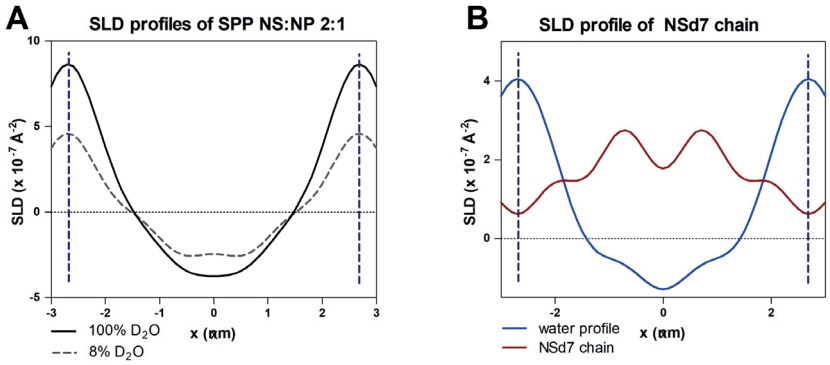

Figure 6. (A) SLD profile of the SPP NS:NP 2:1 sample hydrated at 100% and 8% D_2O/H_2O buffer and (B) SLD water profile (in blue) of the sample and the SLD profile of the CER NSd7 chain (in red). The vertical dashed lines indicate the borders of the repeating unit of the SPP.

CONCLUSION

In this study, the impact of altering the molar ratio of CER NS and CER NP, one of the lipid compositional changes in inflammatory skin diseases, was examined in lipid models that formed exclusively the SPP. The results were compared to previously studied LPP models with the same composition and CER NS:CER NP ratio. In the SPP models, CER NS and CER NP adopt an extended conformation, with the acyl chains of the two CERs in proximity to the FFA C24 chain in the SPP unit, similar to the arrangement described in the LPP unit cell. The different thermotropic behavior reported in the SPP NS:NP 1:2 model and the X-ray diffraction profile indicates that there are lipid domains formed in this system, possibly this is a CER NP-rich phase. Unlike these observations, in LPP models no phase separation is observed, suggesting that the addition of CER EOS improves not only the lipid barrier (33, 35), but also enhances the miscibility of the lipid chains. Moreover, the SPP systems investigated in this study and the corresponding LPP models previously studied showed a different conformational ordering of the lipids. In SPP models with deuterated acyl chain

of CER NS and CER NP and DFFA, the protiated lipids show a higher conformational disordering of the chains compared to the LPP models (at 10°C). This could be due to the acyl chain of CER EOS probably located in the outer layers with the sphingosine and phytosphingosine chains and the CHOL, which improves the lipid ordering in the outer layers of the LPP (44). While some aspects are similar in the SPP and LPP models with different ratios of CER NS:CER NP, the absence of CER EOS affects the mixing of the lipid chains and allows domain formation in models with a high concentration of CER NP. This determines a larger effect when changing the CER NS:CER NP ratio on the lipid organization in SPP models, compared to LPP systems.

ACKNOWLEDGEMENTS

We thank the ALBA Synchrotron (Cerdanyola del Vallès, Spain) and ISIS Neutron and Muon Source (Didcot, United Kingdom) for the experimental beam time to perform the X-ray scattering and neutron diffraction measurements. ISIS data DOI: 10.5286/ISIS.E.RB2069000-1 (68). We are grateful to Evonik (Essen, Germany) for providing the CERs for this study. This study was financially supported by the National Institutes of Health (National Institute of Arthritis and Muscoskeletal and Skin Diseases), grant number R01AR072679.

REFERENCES

1. Hannun, Y. A. (1996). Functions of Ceramide in Coordinating Cellular Responses to Stress. *Science*. 274, 1855-9.
2. Taha, T. A., Mullen, T. D., Obeid, L. M. (2006). A house divided: ceramide, sphingosine, and sphingosine-1-phosphate in programmed cell death. *Biochim Biophys Acta*. 1758(12), 2027-36.
3. Wertz, P. W., Miethke, M. C., Long, S. A., Strauss, J. S., Downing, D. T. (1985). The composition of the ceramides from human stratum corneum and from comedones. *J Invest Dermatol*. 84(5), 410-2.
4. Weerheim, A., Ponec, M. (2001). Determination of stratum corneum lipid profile by tape stripping in combination with high-performance thin-layer chromatography. *Arch Dermatol Res*. 293, 191-9.
5. Madison, K. C. (2003). Barrier function of the skin: "la raison d'etre" of the epidermis. *J Invest Dermatol*. 121(2), 231-41.
6. Proksch, E., Brandner, J. M., Jensen, J.-M. (2008). The skin: an indispensable barrier. *Experimental Dermatology*. 17(12), 1063-72.
7. Ponec, M., Weerheim, A., Lankhorst, P., Wertz, P. (2003). New Acylceramide in Native and Reconstructed Epidermis. *J Invest Dermatol*. 120(4), 581-8.
8. Demel, R. A., de Kruyff, B. (1976). The Function of Sterols in Membranes. *Biochim Biophys Acta*. 457, 109-32.
9. White, S. H., Mirejovsky, D., King, G. I. (1988). Structure of Lamellar Lipid Domains and Corneocyte Envelopes of Murine Stratum Corneum. An X-ray Diffraction Study. *Biochemistry*. 27, 3725-32.
10. Bouwstra, J. A., Gooris, G. S., van der Spek, J. A., Bras, W. (1991). Structural investigations of human stratum corneum by small-angle X-ray scattering. *J Invest Dermatol*. 97(6), 1005-12.
11. Hill, J. R., Wertz, P. W. (2003). Molecular models of the intercellular lipid lamellae from epidermal stratum corneum. *Biochimica et Biophysica Acta (BBA) - Biomembranes*. 1616(2), 121-6.
12. Bouwstra, J. A., Gooris, G. S., Dubbelaar, F. E., Weerheim, A., IJzerman, A. P., Ponec, M. (1998). Role of ceramide 1 in the molecular organization of the stratum corneum lipids. *J Lipid Res*. 39, 186-96.
13. Uche, L. E., Gooris, G. S., Bouwstra, J. A., Beddoes, C. M. (2021). High concentration of the ester-linked omega-hydroxy ceramide increases the permeability in skin lipid model membranes. *Biochim Biophys Acta Biomembr*. 1863(1), 183487.
14. Bouwstra, J. A., Nadaban, A., Bras, W., McCabe, C., Bunge, A., Gooris, G. S. (2023). The skin barrier: An extraordinary interface with an exceptional lipid organization. *Prog Lipid Res*. 101252.
15. Mendelsohn, R., Rerek, M. E., Moore, D. J. (2000). Infrared spectroscopy and microscopic imaging of stratum corneum models and skin. *Physical Chemistry Chemical Physics*. 2(20), 4651-7.
16. Boncheva, M., Damien, F., Normand, V. (2008). Molecular organization of the lipid matrix in intact Stratum corneum using ATR-FTIR spectroscopy. *Biochim Biophys Acta*. 1778(5), 1344-55.
17. Damien, F., Boncheva, M. (2010). The extent of orthorhombic lipid phases in the stratum corneum determines the barrier efficiency of human skin in vivo. *J Invest Dermatol*. 130(2), 611-4.
18. Björklund, S., Nowacka, A., Bouwstra, J. A., Sparr, E., Topgaard, D. (2013). Characterization of Stratum Corneum Molecular Dynamics by Natural-Abundance 13C Solid-State NMR. *PLoS One*. 8(4), e61889.
19. van Smeden, J., Janssens, M., Gooris, G. S., Bouwstra, J. A. (2014). The important role of stratum corneum lipids for the cutaneous barrier function. *Biochim Biophys Acta*. 1841(3), 295-313.
20. Motta, S., Monti, M., Sesana, S., Caputo, R., Carelli, S., Ghidoni, R. (1993). Ceramide composition of the psoriatic scale. *Biochim Biophys Acta*. 1182, 147-51.
21. Janssens, M., van Smeden, J., Gooris, G. S., Bras, W., Portale, G., Caspers, P. J., et al. (2011). Lamellar lipid organization and ceramide composition in the stratum corneum of patients with atopic eczema. *J Invest Dermatol*. 131(10), 2136-8.
22. Sahle, F. F., Gebre-Mariam, T., Dobner, B., Wohlrab, J., Neubert, R. H. (2015). Skin diseases associated with the depletion of stratum corneum lipids and stratum corneum lipid substitution therapy. *Skin Pharmacol Physiol*. 28(1), 42-55.
23. Yokose, U., Ishikawa, J., Morokuma, Y., Naoe, A., Inoue, Y., Yasuda, Y., et al. (2020). The ceramide [NP]/[NS] ratio in the stratum corneum is a potential marker for skin properties and epidermal differentiation. *BMC Dermatology*. 20(1).

24. Uchino, T., Kamiya, D., Yagi, H., Fujino-Shimaya, H., Hatta, I., Fujimori, S., et al. (2023). Comparative analysis of intercellular lipid organization and composition between psoriatic and healthy stratum corneum. *Chem Phys Lipids*. 254, 105305.
25. Rousel, J., Nădăban, A., Saghari, M., Pagan, L., Zhuparris, A., Theelen, B., et al. (2024) Lesional skin of seborrheic dermatitis patients is characterized by skin barrier dysfunction and correlating alterations in the stratum corneum ceramide composition. *Exp. Dermatol.* 33(1), e14952.
26. van Smeden, J., Al-Khakany, H., Wang, Y., Visscher, D., Stephens, N., Absalah, S., et al. (2020). Skin barrier lipid enzyme activity in Netherton patients is associated with protease activity and ceramide abnormalities. *J Lipid Res*. 61(6), 859-69.
27. Nădăban, A., Rousel, J., El Yachioui, D., Gooris, G. S., Beddoes, C. M., Dalgliesh, R. M., et al. (2023). Effect of sphingosine and phytosphingosine ceramide ratio on lipid arrangement and barrier function in skin lipid models. *J Lipid Res*. 64(8), 100400.
28. McIntosh, T. J., Stewart, M. E., Downing, D. T. (1996). X-ray Diffraction Analysis of Isolated Skin Lipids: Reconstitution of Intercellular Lipid Domains. *Biochemistry*. 35(12), 3649-53.
29. Bouwstra, J., Gooris, G., Cheng, K., A., W., Bras, W., Ponec, M. (1996). Phase behavior of isolated skin lipids. *J Lipid Res*. 37, 999 - 1011.
30. Bouwstra, J. A., Gooris, G. S., Dubbelaar, F. E. R., Ponec, M. (2001). Phase behavior of lipid mixtures based on human ceramides: coexistence of crystalline and liquid phases. *J Lipid Res*.42(11), 1759-70.
31. de Jager, M. W., Gooris, G. S., Ponec, M., Bouwstra, J. A. (2005). Lipid mixtures prepared with well-defined synthetic ceramides closely mimic the unique stratum corneum lipid phase behavior. *J Lipid Res*. 46(12), 2649-56.
32. Janssens, M., Gooris, G. S., Bouwstra, J. A. (2009). Infrared spectroscopy studies of mixtures prepared with synthetic ceramides varying in head group architecture: coexistence of liquid and crystalline phases. *Biochim Biophys Acta*. 1788(3), 732-42.
33. Opalka, L., Kovacik, A., Maixner, J., Vavrova, K. (2016). Omega-O-Acylceramides in Skin Lipid Membranes: Effects of Concentration, Sphingoid Base, and Model Complexity on Microstructure and Permeability. *Langmuir*. 32(48), 12894-904.
34. Uche, L. E., Gooris, G. S., Bouwstra, J. A., Beddoes, C. M. (2019). Barrier Capability of Skin Lipid Models: Effect of Ceramides and Free Fatty Acid Composition. *Langmuir*. 35(47), 15376-88.
35. Opálka, L., Kováčik, A., Pullmannová, P., Maixner, J., Vávrová, K. (2020). Effects of omega-O-acylceramide structures and concentrations in healthy and diseased skin barrier lipid membrane models. *J Lipid Res*. 61(2), 219-28.
36. Mojumdar, E. H., Gooris, G. S., Bouwstra, J. A. (2015). Phase behavior of skin lipid mixtures: the effect of cholesterol on lipid organization. *Soft Matter*. 11, 4326-36.
37. Skolova, B., Janusova, B., Zbytovska, J., Gooris, G., Bouwstra, J., Slepicka, P., et al. (2013). Ceramides in the skin lipid membranes: length matters. *Langmuir*. 29(50), 15624-33.
38. Skolova, B., Hudska, K., Pullmannova, P., Kovacik, A., Palat, K., Roh, J., et al. (2014). Different phase behavior and packing of ceramides with long (C16) and very long (C24) acyls in model membranes: infrared spectroscopy using deuterated lipids. *J Phys Chem B*. 118(35), 10460-70.
39. Oguri, M., Gooris, G. S., Bito, K., Bouwstra, J. A. (2014). The effect of the chain length distribution of free fatty acids on the mixing properties of stratum corneum model membranes. *Biochim Biophys Acta*. 1838(7), 1851-61.
40. Engberg, O., Kovacik, A., Pullmannova, P., Juhascik, M., Opalka, L., Huster, D., et al. (2020). The Sphingosine and Acyl Chains of Ceramide [NS] Show Very Different Structure and Dynamics That Challenge Our Understanding of the Skin Barrier. *Angew Chem Int Ed*. 59, 17383 - 7.
41. Gooris, G. S., Kamran, M., Kros, A., Moore, D. J., Bouwstra, J. A. (2018). Interactions of dipalmitoylphosphatidylcholine with ceramide-based mixtures. *Biochim Biophys Acta Biomembr*. 1860(6), 1272-81.
42. Wojdyr, M. (2010). Fityk: a general-purpose peak fitting program. *Journal of Applied Crystallography*. 43(5), 1126-8.
43. Arnold, O., Bilheux, J. C., Borreguero, J. M., Buts, A., Campbell, S. I., Chapon, L., et al. (2014). Mantid—Data analysis and visualization package for neutron scattering andμSR experiments. *Nuclear Instruments and Methods in Physics Research Section A: Accelerators, Spectrometers, Detectors and Associated Equipment*. 764, 156-66.

44. Mojumdar, E. H., Gooris, G. S., Groen, D., Barlow, D. J., Lawrence, M. J., Deme, B., et al. (2016). Stratum corneum lipid matrix: Location of acyl ceramide and cholesterol in the unit cell of the long periodicity phase. *Biochim Biophys Acta*. 1858(8), 1926-34.
45. Franks, N. P., Lieb, W.R. (1979). The Structure of Lipid Bilayers and the Effects of General Anaesthetics: An X-ray and Neutron Diffraction Study. *J Mol Biol*. 133, 469-500.
46. Nădăban, A., Gooris, G. S., Beddoes, C. M., Dalgliesh, R. M., Bouwstra, J. A. (2022). Phytosphingosine ceramide mainly localizes in the central layer of the unique lamellar phase of skin lipid model systems. *J Lipid Res*. 63(9), 100258.
47. NIST Center of Neutron Research, https://www.ncnr.nist.gov/resources/activation/ (Accessed: 2021).
48. Wiener, M. K., G.; White, S. (1991). Structure of a fluid dioleoylphosphatidylcholine bilayer determined by joint refinement of x-ray and neutron diffraction data 1. Scaling of neutron data and the distributions of double bonds and water. *Biophys J*. 60, 568-76.
49. Mojumdar, E. H., Gooris, G. S., Barlow, D. J., Lawrence, M. J., Deme, B., Bouwstra, J. A. (2015). Skin lipids: localization of ceramide and fatty acid in the unit cell of the long periodicity phase. *Biophys J*. 108(11), 2670-9.
50. Kovacik, A., Vogel, A., Adler, J., Pullmannova, P., Vavrova, K., Huster, D. (2018). Probing the role of ceramide hydroxylation in skin barrier lipid models by (2)H solid-state NMR spectroscopy and X-ray powder diffraction. *Biochim Biophys Acta Biomembr*. 1860(5), 1162-70.
51. Kovacik, A., Silarova, M., Pullmannova, P., Maixner, J., Vavrova, K. (2017). Effects of 6-Hydroxyceramides on the Thermotropic Phase Behavior and Permeability of Model Skin Lipid Membranes. *Langmuir*. 33(11), 2890-9.
52. Pullmannova, P., Ermakova, E., Kovacik, A., Opalka, L., Maixner, J., Zbytovska, J., et al. (2019). Long and very long lamellar phases in model stratum corneum lipid membranes. *J Lipid Res*. 60(5), 963-71.
53. Pullmannova, P., Curikova-Kindlova, B. A., Ondrejcekova, V., Kovacik, A., Dvorakova, K., Dulanska, L., et al. (2023). Polymorphism, Nanostructures, and Barrier Properties of Ceramide-Based Lipid Films. *ACS Omega*. 8(1), 422-35.
54. Parrott, D. T., Turner, J. E. (1993). Mesophase formation by ceramides and cholesterol: a model for stratum corneum lipid packing? *Biochim Biophys Acta*. 1147, 273 - 6.
55. Dahlen, B., Pascher, I. (1979). Molecular arrangements in sphingolipids. Thermotropic phase behaviour of tetracosanoylphytosphingosine. *Chem Phys Lipids*. 24, 119 - 33.
56. Schroeter, A., Stahlberg, S., Skolova, B., Sonnenberger, S., Eichner, A., Huster, D., et al. (2017). Phase separation in ceramide[NP] containing lipid model membranes: neutron diffraction and solid-state NMR. *Soft Matter*. 13(10), 2107-19.
57. de Jager, M., Gooris, G., Ponec, M., Bouwstra, J. (2004). Acylceramide head group architecture affects lipid organization in synthetic ceramide mixtures. *J Invest Dermatol*. 123(5), 911-6.
58. Moore, D. J., Rerek, M. E., Mendelsohn, R. (1997). FTIR Spectroscopy Studies of the Conformational Order and Phase Behavior of Ceramides. *J Phys Chem B*. 101, 8933-40.
59. Moore, D. J., Rerek, M. E., Mendelsohn, R. (1999). Role of ceramides 2 and 5 in the structure of the stratum corneum lipid barrier. *Int J Cosmet Sci*. 21(5), 353-68.
60. Rerek, M. E., Chen, H., Markovic, B., Van Wyck, D., Garidel, P., Mendelsohn, R., et al. (2001). Phytosphingosine and Sphingosine Ceramide Headgroup Hydrogen Bonding: Structural Insights through Thermotropic Hydrogen/Deuterium Exchange. *J Phys Chem B*. 105, 9355 - 62.
61. Uche, L. E., Gooris, G. S., Beddoes, C. M., Bouwstra, J. A. (2019). New insight into phase behavior and permeability of skin lipid models based on sphingosine and phytosphingosine ceramides. *Biochim Biophys Acta Biomembr*. 1861(7), 1317-28.
62. de Sousa Neto, D., Gooris, G., Bouwstra, J. (2011). Effect of the omega-acylceramides on the lipid organization of stratum corneum model membranes evaluated by X-ray diffraction and FTIR studies (Part I). *Chem Phys Lipids*. 164(3), 184-95.
63. Moore, D. J., Rerek, M. E., Mendelsohn, R. (1997). Lipid Domains and Orthorhombic Phases in Model Stratum Corneum: Evidence from Fourier Transform Infrared Spectroscopy Studies. *Biochemical and Biophysical Research Communications*. 231, 797 - 801.

64. Mendelsohn, R., Moore, D. J. (1998). Vibrational spectroscopic studies of lipid domains in biomembranes and model systems. *Chem Phys Lipids*. 96, 141-57.
65. Beddoes, C. M., Gooris, G. S., Bouwstra, J. A. (2018). Preferential arrangement of lipids in the long-periodicity phase of a stratum corneum matrix model. *J Lipid Res*. 59(12), 2329-38.
66. Beddoes, C. M., Gooris, G. S., Foglia, F., Ahmadi, D., Barlow, D. J., Lawrence, M. J., et al. (2020). Arrangement of Ceramides in the Skin: Sphingosine Chains Localize at a Single Position in Stratum Corneum Lipid Matrix Models. *Langmuir*. 36(34), 10270-8.
67. Schmitt, T., Lange, S., Dobner, B., Sonnenberger, S., Hauss, T., Neubert, R. H. H. (2018). Investigation of a CER[NP]- and [AP]-Based Stratum Corneum Modeling Membrane System: Using Specifically Deuterated CER Together with a Neutron Diffraction Approach. *Langmuir*. 34(4), 1742-9.
68. Bouwstra, J. A., Beddoes, C. M., Nădăban, A., Dalgliesh, R. M., Gooris, G. S. (2020) The effect of ceramide head group on the lipid organization in the long periodicity phase of stratum corneum substitutes. STFC ISIS Neutron and Muon Source. DOI: https://doi.org/ 10.5286/ISIS.E.RB2069000.

SUPPLEMENTAL INFORMATION

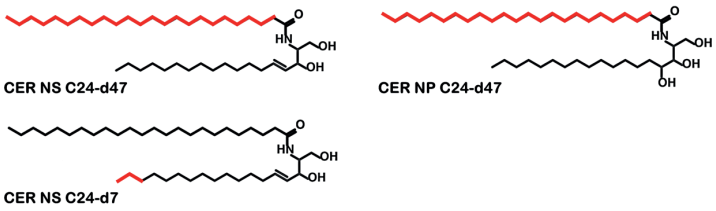

Figure S1. The molecular structure of the CERs used in this study. The deuterated moieties are depicted in red (the acyl chains of CER NS and CER NP and the terminally deuterated sphingosine chain of CER NS).

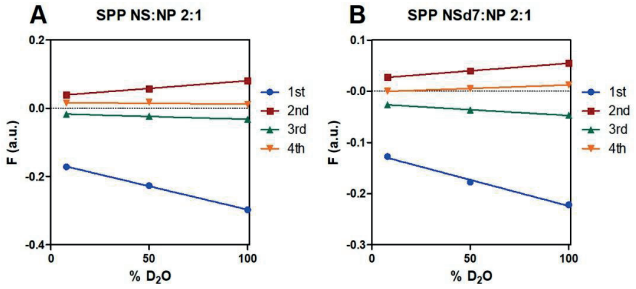

Figure S2. Linear fitting of the structure factors as a function of the percentage of D_2O in the D_2O/H_2O buffer for the SPP NS:NP 2:1 model and SPP NSd7:NP 2:1 models. The four diffraction orders are indicated by different symbols and colors: first (dot, blue), second (square, red), third (triangle, green), fourth (triangle, orange).

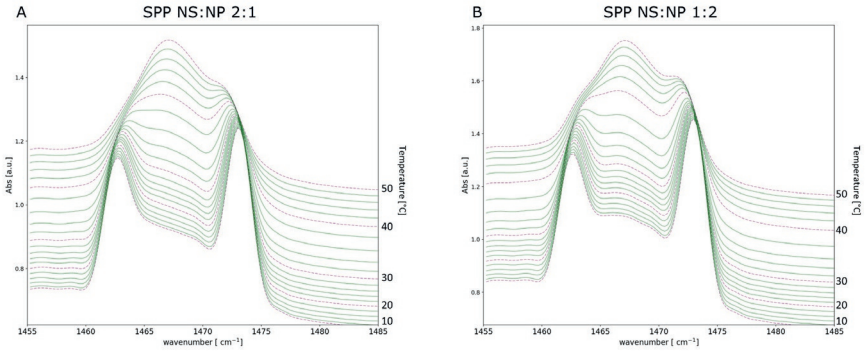

Figure S3. The δCH_2 vibrations of the SPP NS:NP 2:1 (A) and SPP NS:NP 1:2 (B) models, measured in the temperature range 10 – 50 °C.

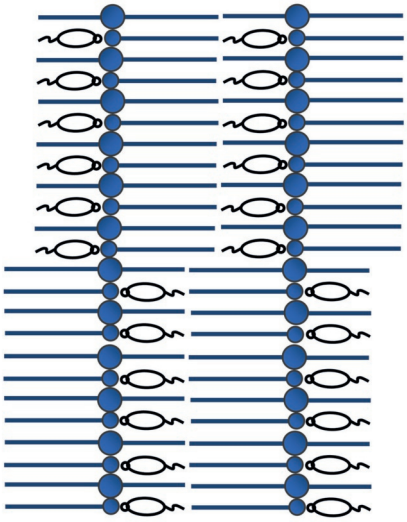

Figure S4. Proposed schematic model for the arrangement of the SPP unit cell. CHOL is shown in black, FFA is indicated as a single acyl chain in blue and the CER is depicted in blue, in an extended conformation (the acyl chain and sphingoid base on each side of the head group). The asymmetric structure mirrors itself within the lamellar structure, resulting in a symmetric structure of the SPP unit.